ADVANCES IN ATMOSPHERIC SCIENCES, VOL. 35, AUGUST 2018, 1063–1076

• **Original Paper** •

Representation of the ENSO Combination Mode and its Asymmetric SST Response in Different Resolutions of HadGEM3

Jianghua WAN[1], Hongli REN[*1,2], and Peili WU[3]

[1] *Laboratory for Climate Studies, and CMA-NJU Joint Laboratory for Climate Prediction Studies, National Climate Center, China Meteorological Administration, Beijing* 100081*, China*

[2] *Department of Atmospheric Sciences, School of Environment Studies University of Geoscience, Wuhan* 430074*, China*

[3] *Met Office Hadley Center, Exeter* EX1 3PB*, UK*

(Received 15 November 2017; revised 27 April 2018; accepted 2 May 2018)

ABSTRACT

Previous studies have revealed a combination mode (C-mode) occurring in the Indo-Pacific region, arising from nonlinear interactions between ENSO and the western Pacific warm pool annual cycle. This paper evaluates the simulation of this C-mode and its asymmetric SST response in HadGEM3 and its resolution sensitivity using three sets of simulations at horizontal resolutions of N96, N216 and N512. The results show that HadGEM3 can capture well the spatial pattern of the C-mode associated surface wind anomalies, as well as the asymmetric response of SST in the tropical Pacific, but it strongly overestimates the explained variability of the C-mode compared to the ENSO mode. The model with the three resolutions is able to reproduce the distinct spectral peaks of the C-mode at the near annual combination frequencies, but the performance in simulating the longer periods is not satisfactory, presumably due to the unrealistic simulation of the ENSO mode. Increasing the horizontal resolution can improve the consistency between atmospheric and oceanic representations of the C-mode, but not necessarily enhance the accuracy of C-mode simulation compared with observation.

Key words: ENSO combination mode, asymmetric response, Niño-A index, HadGEM3, horizontal resolution

Citation: Wan, J. H., H. L. Ren, and P. L. Wu, 2018: Representation of the ENSO combination mode and its asymmetric SST response in different resolutions of HadGEM3. *Adv. Atmos. Sci.*, **35**(8), 1063–1076, https://doi.org/10.1007/s00376-018-7285-5.

1. Introduction

The El Niño–Southern Oscillation (ENSO) is a dominant mode of interannual climate variability and has pronounced impacts on global climate (Ropelewski and Halpert, 1987; Trenberth et al., 1998; Wallace et al., 1998; Trenberth and Caron, 2000). Recent studies have shown that nonlinear interactions between ENSO and the background western Pacific warm pool annual cycle can generate an ENSO/annual cycle combination mode (C-mode) (Stuecker et al., 2013), which exhibits pronounced variability of near-annual combination tone periods at ~10 and ~15 months. Besides, it demonstrates distinct meridionally asymmetric patterns related to the equator in atmospheric variables (Stuecker et al., 2013, 2015a, 2015b), as well as SST anomalies (Zhang et al., 2016b).

This C-mode over the Pacific warm pool plays an important role in the ENSO life cycle by contributing to the southward shift of anomalous central Pacific low-level zonal winds during the rapid termination of El Niño events (Harrison and Vecchi, 1999; Vecchi, 2006; McGregor et al., 2012; Stuecker et al., 2013). In addition, it plays a considerable part in the developing and maintaining processes of the anomalous low-level Northwest Pacific anticyclone (Stuecker et al., 2015b). A distinguished annual-cycle modulation of the meridional asymmetry in the atmospheric response to Eastern Pacific El Niño events has been detected, which does not emerge in Central Pacific El Niño or La Niña events (Zhang et al., 2015; Zhang et al., 2016b). Moreover, the C-mode may significantly affect East Asian precipitation anomalies and remarkably improve the predictability of Yangtze River basin summer rainfall (Li et al., 2016a; Zhang et al., 2016a, 2016b).

Considering the C-mode is crucial for both ENSO seasonally modulated dynamics and the ENSO climatic influence in the tropical Pacific to the western North Pacific, it is of great importance to evaluate the performances of models in simulating the C-mode. Li et al. (2016b) found the southward shift of the anomalous westerly over the central Pacific might only occur with the annual cycle background in an AGCM. Zhang et al. (2016b) evaluated the predictive skill of the oceanic C-mode in five dynamical models that participated in Weisheimer et al. (2009), and found it to be lower

---

[*] Corresponding author: Hongli REN
Email: renhl@cma.gov.cn

than that for the Niño3.4 index. Ren et al. (2016) assessed the performance of capturing the observed C-mode characteristics in 27 CGCMs from CMIP5. Most of the coupled climate models in CMIP5 are able to reproduce the spatial pattern of the C-mode well in terms of the surface wind variability, and about half can reproduce the spectral power at the combination tone periodicities. In this study, both the atmospheric aspect and the oceanic response of the combination mode were examined in a model simulation, and the sensitivity to model resolution was discussed.

2. Data and methods

The climate model used in this study is HadGEM3-GC2, which is the latest version of the UK Met Office Hadley Centre's coupled climate modeling system. It consists of the Met Office's Unified Model as the atmospheric component, JULES as the land-surface component, NEMO as the ocean component, and CICE as the sea-ice model. More details of the model can be found in Hewitt et al. (2011), Williams et al. (2015) and Senior et al. (2016). We utilized three different horizontal resolution configurations to look at the sensitivity of the C-mode simulation to the resolution. The N96 horizontal resolution is 1.25° latitude ×1.875° longitude, which is approximately 130 km at the surface. N216 is 0.8° latitude ×0.5° longitude (approximately 60 km at the surface), and N512 is approximately 25 km. The fully coupled model was integrated for 61 years at each resolution.

For comparison, we utilized the monthly 10-m wind data from the NCEP–NCAR reanalysis dataset (1961–2015) (Kalnay et al., 1996), NCEP–DOE data, ERA-40 data, and 20CR data. The SST anomalies (1961–2011) associated with ENSO and the C-mode are examined using the HadISST1 dataset, provided by the UK Met Office (Rayner et al., 2003), as well as the OISST and ERSST datasets. The precipitation data are from CMAP.

The ENSO C-mode was derived following the same approach as in Stuecker et al. (2013). We first conduct a combined empirical orthogonal function (EOF) analysis on the anomalous zonal and meridional wind anomalies over the tropical Pacific region (10°S–10°N, 100°E–60°W), and then regress the horizontal wind anomalies onto the first two normalized principal components (PCs), respectively. The oceanic aspect of the C-mode can be represented by the Niño-Asymmetry SST index (Niño-A index), which can comprehensively capture both the meridional asymmetry and the zonal SST asymmetry (Zhang et al., 2016b). The Niño-A index is defined as

$$\text{Niño} - \text{A} = 0.5[\text{SSTA}]_{\text{sw}} + 0.5[\text{SSTA}]_{\text{SE}} - [\text{SSTA}]_{\text{NC}} ,$$

where the brackets denote the area-averaged SST anomalies over the regions SW (0°–20°S, 120°–160°E), SE (0°–20°S, 100°–140°W), and NC (0°–20°N, 150°E–130°W). The Niño3.4 index is defined as the SST anomalies averaged over the region (5°S–5°N, 120°–170°W).

3. Results

3.1. *Characteristics of the C-mode in the reanalysis data*

3.1.1. *Atmospheric features of the C-mode*

Figure 1 displays the first two leading EOF patterns of tropical Pacific surface wind anomalies in different reanalysis products. The datasets show considerable agreement with one another. The first EOF pattern (EOF1) is characterized by a meridionally quasi-symmetric wind distribution with equatorial westerly anomalies over the western-central Pacific, which describes the anomalous Walker circulation associated with ENSO (Figs. 1a, c, e and g). The second EOF mode (EOF2) exhibits a meridionally antisymmetric circulation with a distinct anomalous Northwest Pacific anticyclone and southward shift of the equatorial central-Pacific westerly wind anomalies (Figs. 1b, d, f and h), which is the characteristic atmospheric response to the C-mode (Stuecker et al., 2013, 2015b).

The PC time series are also highly correlated among the different reanalysis datasets (Fig. 2). The correlation coefficient of the PCs between each dataset and the NCEP–NCAR data is higher than 0.9, except for the PC2 between ERA-40 and NCEP–NCAR, which still reaches 0.84. Hereinafter, we use the NCEP–NCAR reanalysis data to validate the model simulation of the C-mode atmospheric variability.

The PC1 time series is highly correlated ($r = 0.85$) with the Niño3.4 index (Fig. 3a), further verifying that EOF1 captures the main ENSO mode in the reanalysis. To better understand the relationship between the ENSO mode and the combination mode, we followed Stuecker et al. (2013) to utilize a theoretical approximation to the C-mode time series by multiplying PC1 by a sinusoidal function with the annual cycle; that is,

$$\text{PC1cos} = \text{PC1}_{\text{obs}}(t) \times \cos(\omega_a t - \varphi) .$$

The ω_a in this equation denotes the angular frequency of the annual cycle, t denotes time and φ represents a one-month shift. This time series represents the combination tones of the ENSO signal and the annual cycle by its mathematical nature. In the reanalysis, PC1cos shows remarkable agreement with the observed PC2 (Fig. 3b). The correlation coefficient is 0.63.

To further understand the combination tones, we calculate the power density spectra for both the PC1 and PC2 time series in the reanalysis (Fig. 4a). The spectrum for PC1 exhibits pronounced levels of variability, mostly in the interannual period band of 2–8 years, while PC2 exhibits a significant spectral peak at a period of ~15 months and a weaker one at ~10 months. Actually, these two peaks align well with the two shifted frequency bands of ENSO-annual cycle combination tones, which is the sum tone as $1 + f_{\text{E}}$ and the difference tone as $1 - f_{\text{E}}$, where f_{E} denotes the ENSO characteristic interannual frequency band.

3.1.2. *Asymmetric SST response of the C-mode*

Besides the surface atmospheric response of the C-mode, the nonlinear processes in the ocean–atmosphere coupled

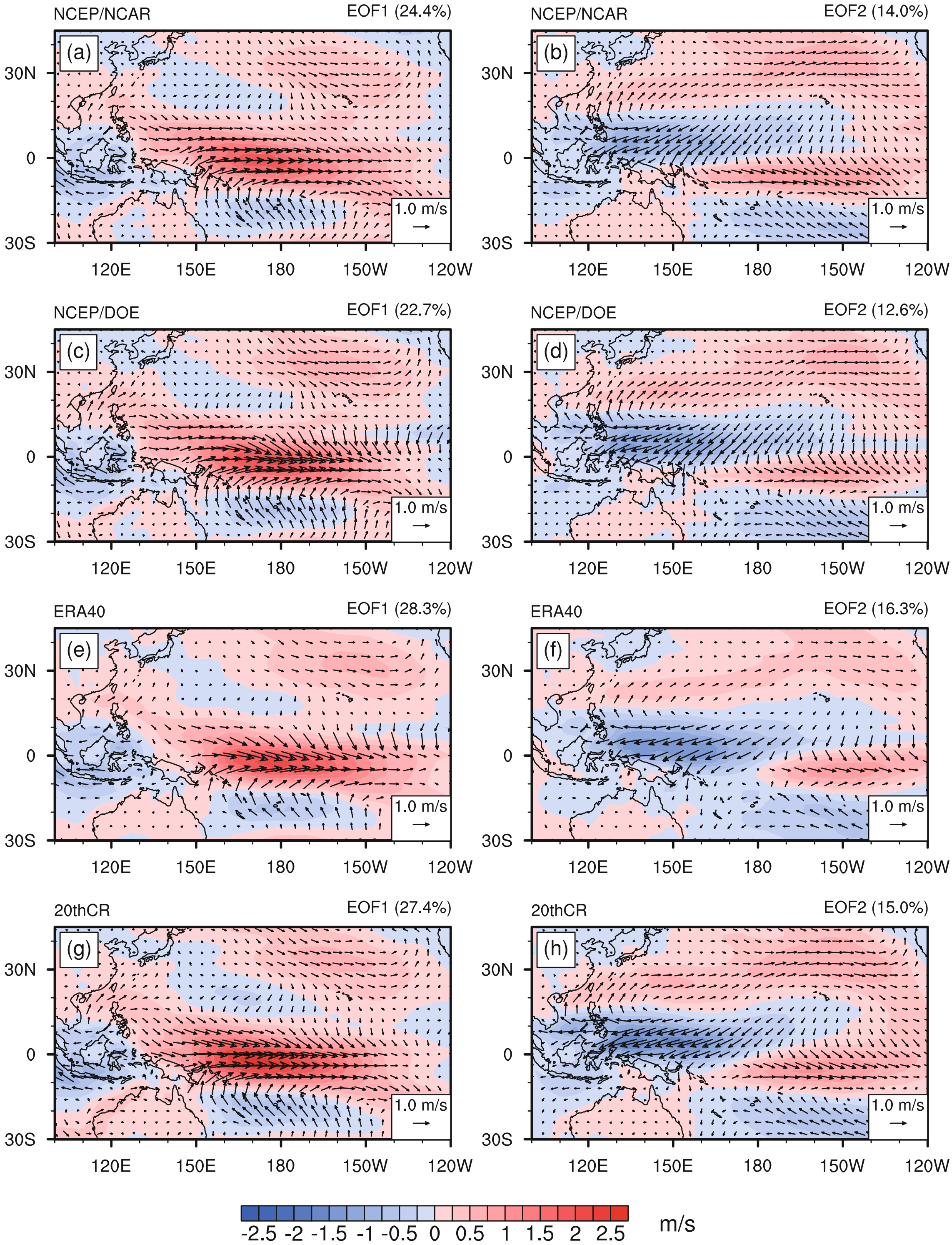

Fig. 1. The leading two EOF spatial patterns of tropical Pacific surface wind anomalies (units: m s^{-1}) for (a, b) NCEP–NCAR, (c, d) NCEP–DOE, (e, f) ERA-40 and (g, h) 20CR. Shading indicates the regressed zonal wind anomalies. Percentages of variance explained by the EOF patterns are given in parentheses.

system may also result in combination tones in oceanic variables (Jin et al., 1994; Stein et al., 2014). Zhang et al. (2016b) pointed out the Niño-A index can capture the SST response to the C-mode very well. Figure 5 demonstrates the SST anomalies and 850-hPa horizontal wind anomalies regressed onto the Niño3.4 and Niño-A indices in different observational datasets. The spatial SST distribution related to ENSO is characterized as a meridionally symmetrical SSTA pattern (Figs. 5a, c and e). Also, the Niño-A index–associated SST anomaly pattern exhibits negative SST anomalies over

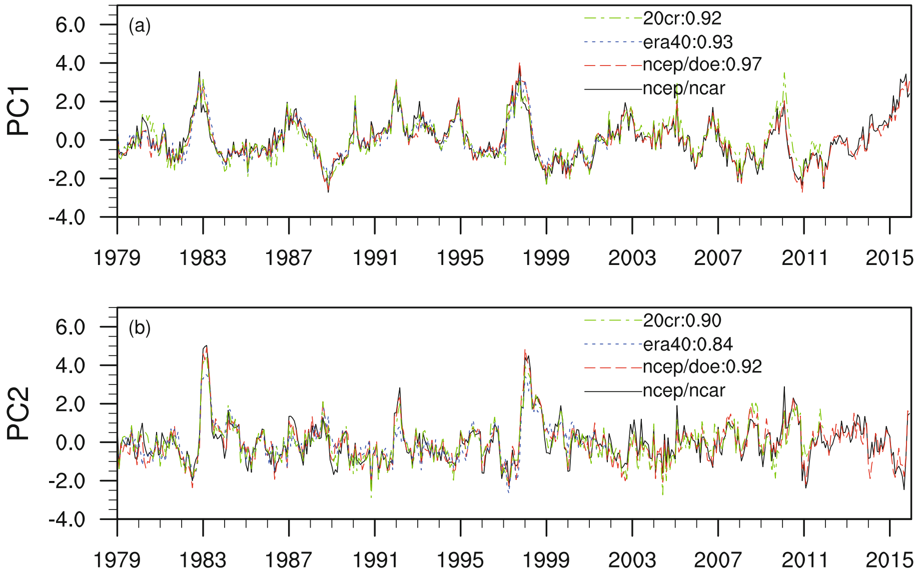

Fig. 2. (a) PC1 and (b) PC2 in different reanalysis datasets. Numbers after the colon are the correlation coefficients between each dataset and the NCEP–NCAR reanalysis.

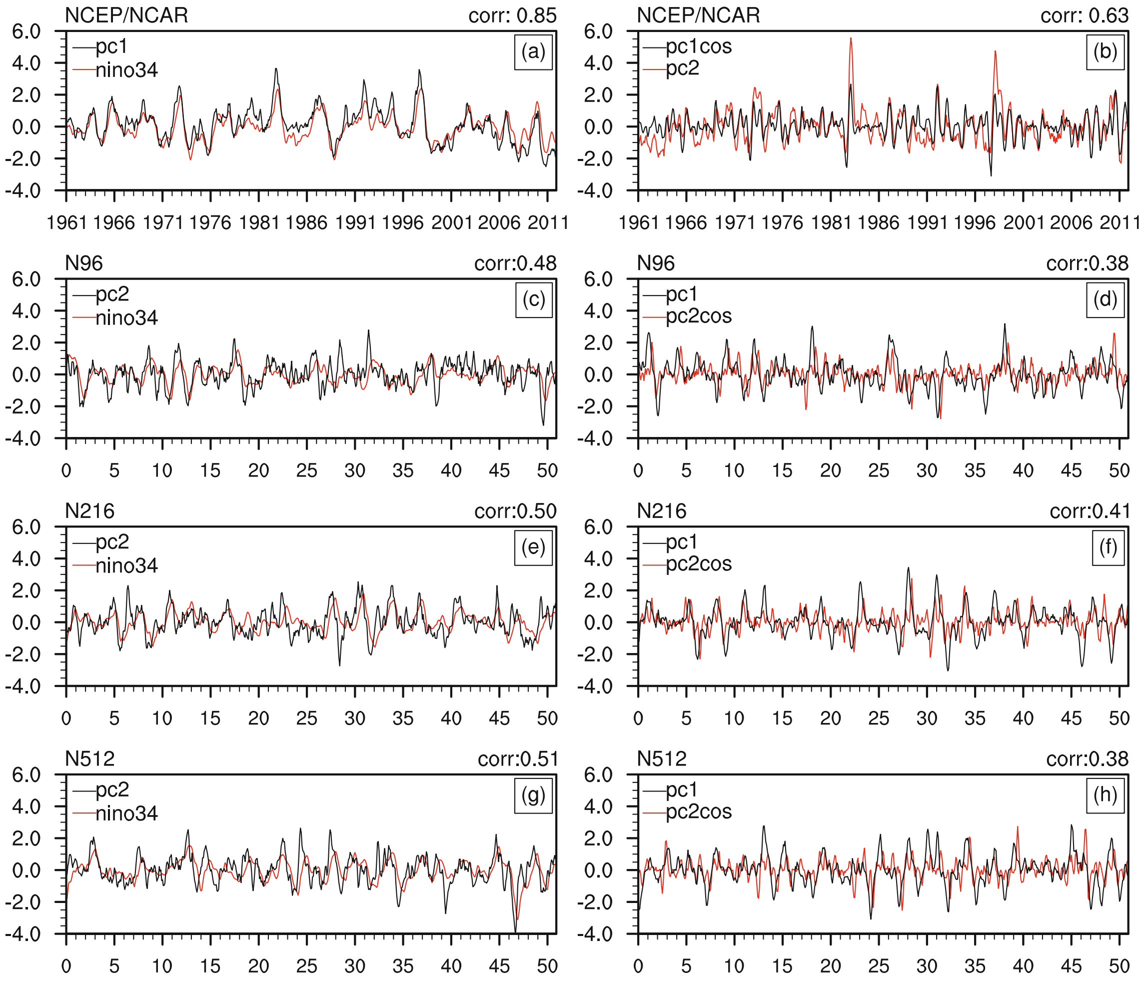

Fig. 3. (a) PC1 and Niño3.4 index for the reanalysis; (b) PC1cos and PC2 for the reanalysis. PC2 and Niño3.4 indices for models at (c) N96, (e) N216 and (g) N512. PC1 and PC2cos for models at (d) N96, (f) N216 and (h) N512. Correlation coefficients between two curves are given in the top right.

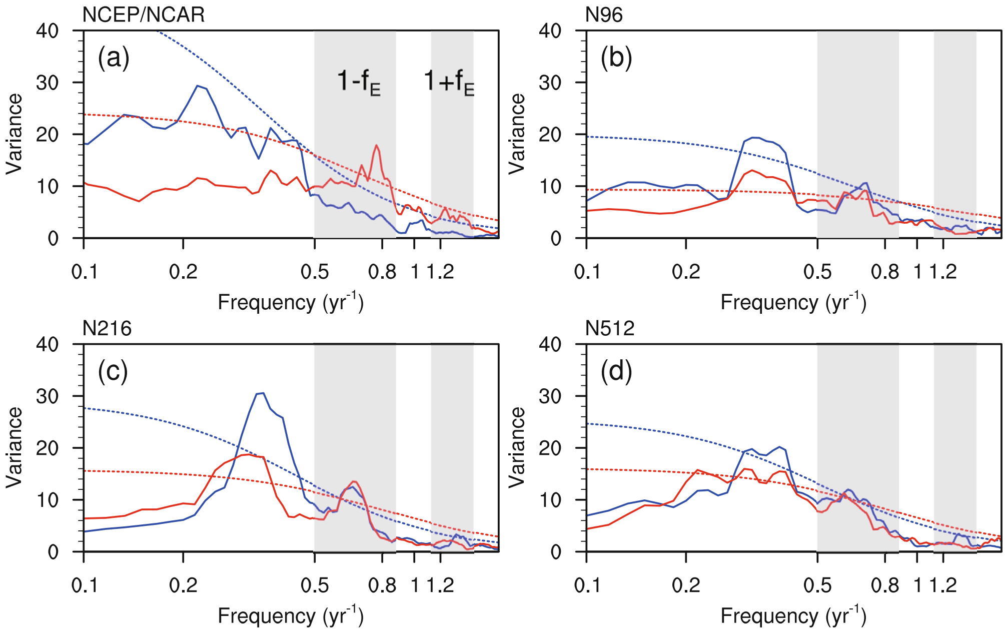

Fig. 4. Spectra curves of PC1 (blue) and PC2 (red), where the dashed lines indicate the statistical significance at the 95% confidence level. Grey rectangles indicate the near-annual combination tone frequency bands.

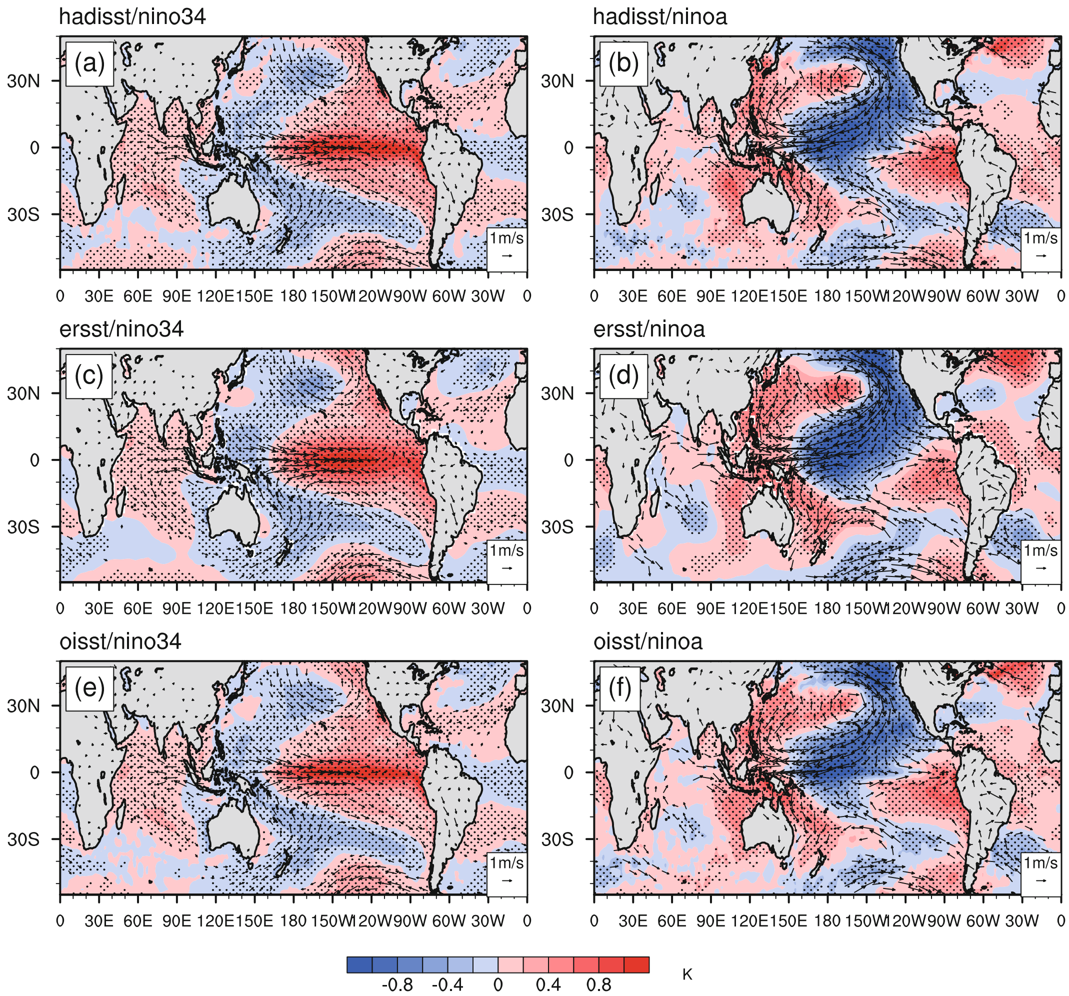

Fig. 5. SST (contours; units: K) and 850-hPa wind (vectors; units: m s^{-1}) anomalies regressed onto the Niño3.4 (left panels) and Niño-A (right panels) indices for (a, b) HadISST, (c, d) ERSST and (e, f) OISST data. Black dots represent the 99% confidence level of the SST. Only regions with at least either of the two components of wind at the 95% confidence level are shown.

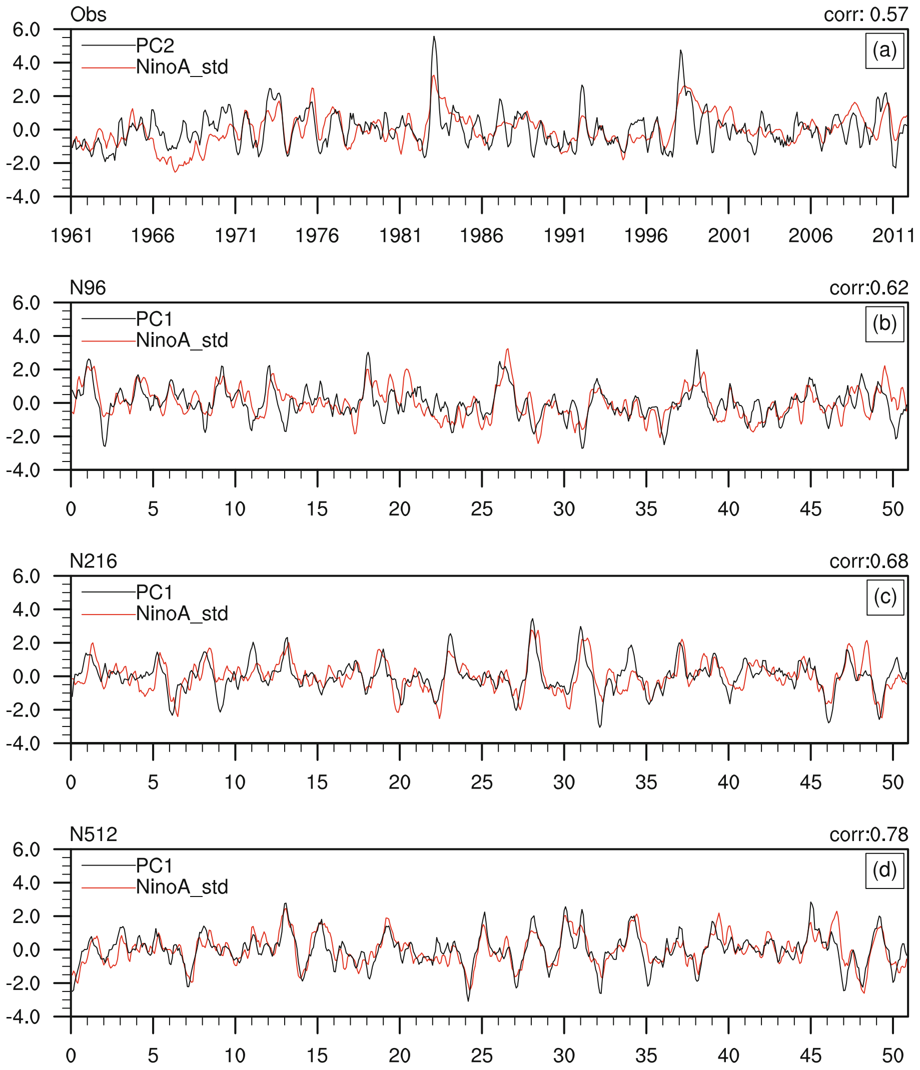

Fig. 6. (a) PC2 (NCEP–NCAR dataset) and standardized Niño-A (HadISST dataset) indices for the observation. (b–d) PC1 and standardized Niño-A indices for model outputs. Correlation coefficients between two curves are given in the top right.

the northern central tropical Pacific and positive SST anomalies over the southwestern and southeastern tropical Pacific (Figs. 5b, d and f), which exhibits a very similar structure to the forced C-mode SST pattern (Zhang et al., 2016b). The anomalous anticyclone over northwestern Pacific can be seen more clearly in the 850-hPa wind field. The results of different observational datasets also show great similarity. We use the HadISST dataset to validate the model simulation of the C-mode oceanic variability afterwards.

The Niño-A index is highly correlated with the PC2 in the reanalysis data (Fig. 6a), verifying it represents the oceanic features of the C-mode. The spectral analysis indicates that the Niño3.4 index spectrum shows a significant 2–8-year peak, and the Niño-A index peaks at combination tone periods of ~10 months and ~15 months (Fig. 7a), which is in agreement with Fig. 4. This implies the Niño-A index also exhibits the combination tone frequency based on the ENSO period and the annual cycle.

3.2. *Simulated C-mode in different model resolutions*

3.2.1. *Simulated spatial patterns of the C-mode*

If we compare the first two leading EOFs simulated by HadGEM3 (Fig. 8) with the corresponding patterns in the reanalysis (Fig. 1), they show significantly different spatial distributions. Unlike the equatorially symmetric EOF1 in the reanalysis, the EOF1 patterns in all three versions of the model exhibit remarkable meridionally antisymmetric structures, with strong shear of anomalous zonal wind across the equator, which bears great resemblance to the EOF2 pattern in the reanalysis, although the anomalous Philippine anticyclones in the models are weaker than in the reanalysis. Meanwhile, the EOF2 patterns in the models show a meridionally symmetric feature, resembling the EOF1 rather than the EOF2 pattern in the reanalysis.

This reversed similarity relationship can be more directly seen in Table 1. The pattern correlation coefficients of the

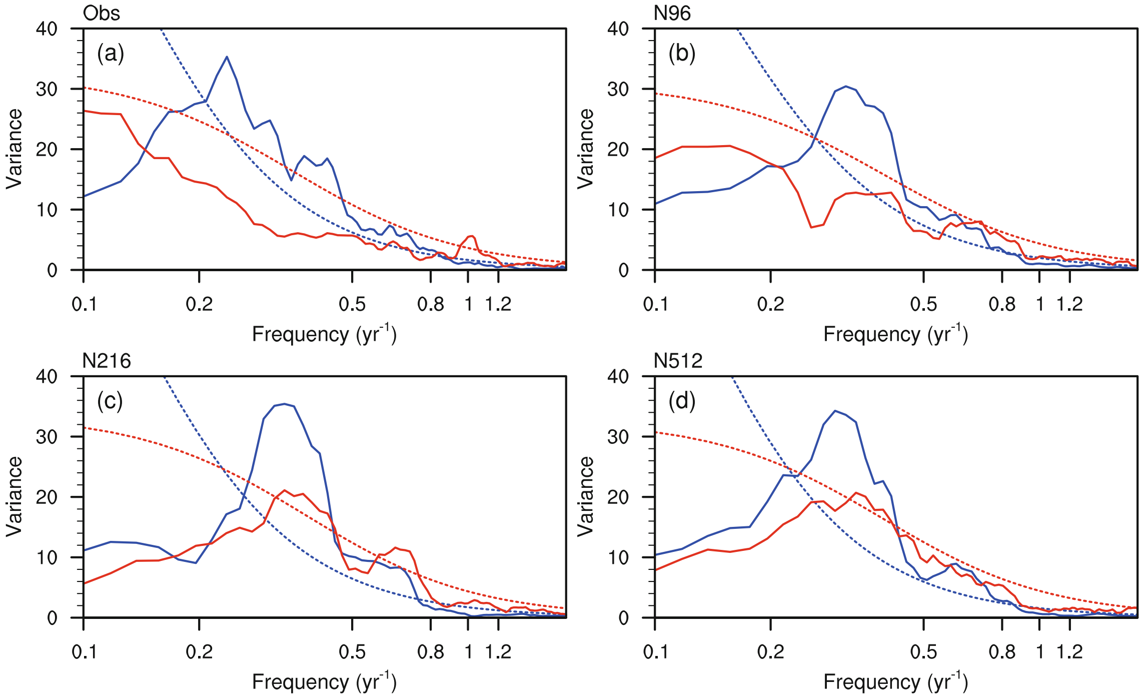

Fig. 7. Spectra curves of standardized Niño3.4 (blue) and Niño-A (red) for the observation and model results. Dashed lines indicate the statistical significance at the 95% confidence level.

same EOF patterns between the models and the NCEP–NCAR reanalysis are very low, with an absolute value of ~0.25 in the case of EOF2. On the other hand, they get much higher when we switch the order of the compared observed EOF. The correlation coefficient between the N96-simulated EOF2 and the observed EOF1 can reach 0.79, and it becomes slightly lower as the resolution gets higher. Moreover, models with better ability to reproduce the ENSO mode can also simulate the C-mode spatial pattern more realistically, which is in accordance with the CMIP5 results (Ren et al., 2016). The results indicate that HadGEM3 can capture the spatial structures of the ENSO mode and the C-mode in the surface wind field. However, it tends to emphasize the C-mode component too much, such that the C-mode turns into the dominant pattern in the tropical Pacific surface wind variability, instead of the ENSO mode as in the reanalysis.

3.2.2. *Simulated combination tone features*

As mentioned above, the ENSO mode in the simulation is represented by EOF2 instead of EOF1; thus, we compare the PC2 in the simulation with the Niño3.4 indices. They agree with each other well, with correlation coefficients around 0.5 in all three simulations (Figs. 3c, e and g). The correlation coefficients grow slightly higher as the model resolution gets higher, which is opposite to the spatial pattern trend (Table 1).

Table 1. Pattern correlation coefficients between the first two leading EOF patterns in the models and reanalysis. The letter "m" in parentheses denotes the EOF of models, and "r" stands for the reanalysis, which is the NCEP–NCAR dataset in this table.

Resolution	EOF1(m)–EOF1(r)	EOF2(m)–EOF2(r)	EOF1(m)–EOF2(r)	EOF2(m)–EOF1(r)
N96	0.44	−0.25	0.66	0.79
N216	0.51	−0.28	0.64	0.75
N512	0.48	−0.24	0.62	0.74

For the model theoretical approximation to the C-mode time series, a similar method was applied, except we used PC2 as the ENSO signal and the theoretical C-mode signal was PC2cos. The PC1s are also well correlated with the theoretical C-mode time series (Figs. 3d, f and h). The middle resolution (N216) model shows the best performance, with the correlation coefficient reaching 0.41. However, the spectra of the first two leading PCs in the model simulation are difficult to distinguish from each other (Figs. 4b, c and d). The ENSO signal (PC2) peaks around the 2–8-year period bands, but also exhibits high-frequency signals, especially at the $1 - f_{\mathrm{E}}$ frequency band. This is notable in the left-hand panel of Fig. 3, in which the PC2s contain detectable high-frequency variability compared with either the PC1 in the reanalysis or the Niño3.4 indices in the simulation. The combination tones (PC1) can capture the $1 - f_{\mathrm{E}}$ and $1 + f_{\mathrm{E}}$ frequency peaks well, but they also show a significant peak in the ENSO mode characteristic low-frequency band, which is not the case in the reanalysis (Fig. 4a).

3.2.3. *Asymmetric SST response of the C-mode in the simulation*

Figure 9 demonstrates the SST anomalies and 850-hPa horizontal wind anomalies regressed onto the Niño3.4 and Niño-A indices in the simulations. All three configurations

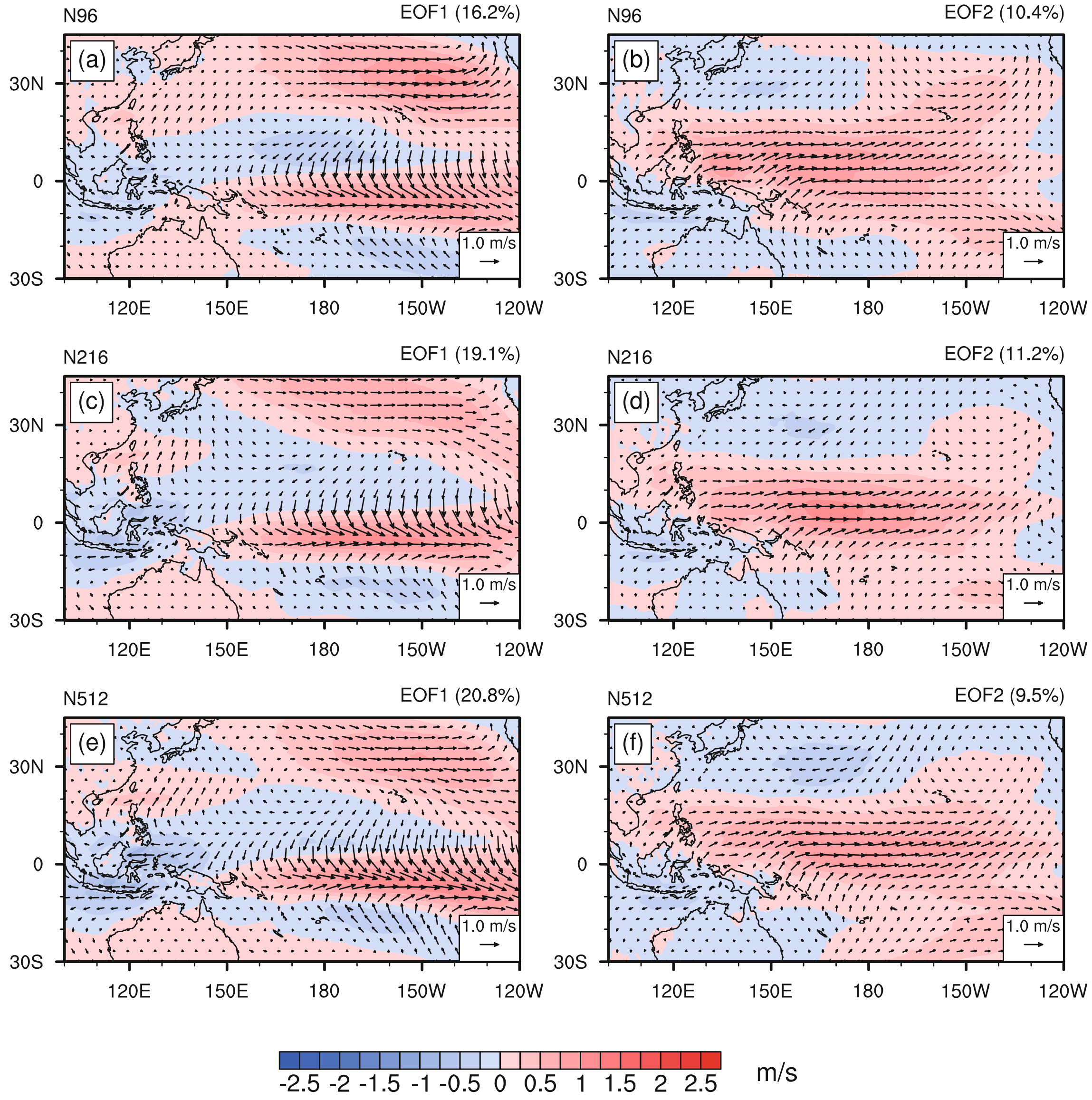

Fig. 8. The leading two EOF spatial patterns of tropical Pacific surface wind anomalies (units: m s^{-1}) for HadleyGEM3 with different resolutions of (a, b) N96, (c, d) N216 and (e, f) N512. Shading indicates the regressed zonal wind anomalies. Percentages of variance explained by the EOF patterns are given in parentheses.

of the model can capture the spatial SST distribution related to the ENSO mode and the C-mode very well, although the C-mode-related warm center over the eastern Pacific is stronger and extends to the central Pacific compared to the observation. The Niño-A index is highly correlated with the PC1s in the model simulations (Figs. 6b–d). The correlation coefficients get higher as the resolution gets higher, which reaches 0.78 in the N512 simulation. This is similar to the relationship between the Niño3.4 index and PC2 in the simulation, as illustrated in the left-hand panel of Fig. 3. This implies that, for both the ENSO mode and C-mode, the atmospheric responses (PCs) are more consistent with the oceanic responses (Niño indices) as the model resolution gets finer.

We also investigate the power spectra of the Niño3.4 and Niño-A indices in the simulations (Figs. 7b–d). In agreement with Fig. 4, the simulated Niño3.4 and Niño-A spectra show a similar performance to PC1 and PC2; the peak frequency bands are overlapped, and therefore they are not easily distinguishable from each other.

3.2.4. *Possible mechanism of the model misrepresentation*

The C-mode emerges from the nonlinear interaction between the ENSO mode and the annual cycle background. It plays an important role in ENSO's phase-lock feature by being responsible for the sudden weakening and southward shift of equatorial westerly anomalies during the termination process of strong El Niño events (Stuecker et al., 2013). We evaluate the phase relationship between PC1 and PC2 by compositing the PCs with respect to the annual cycle evolution for the El Niño events selected by the Niño3.4 indices of

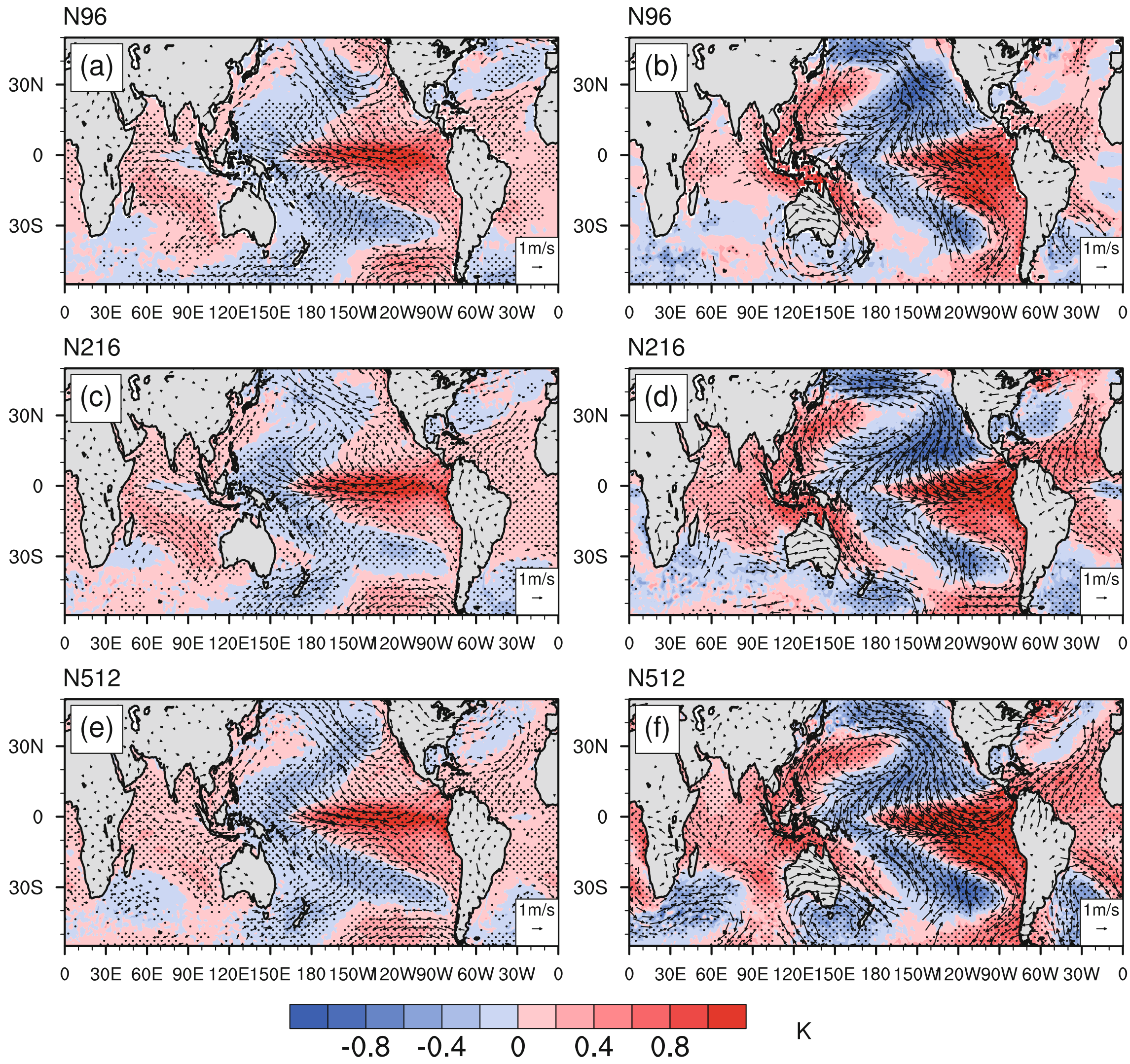

Fig. 9. SST (contours; units: K) and 850-hPa wind (vectors; units: m s^{-1}) anomalies regressed onto the Niño3.4 (left panels) and Niño-A indices (right panels) for the model results at three resolutions. Black dots represent the 99% confidence level of the SST. Only regions with at least either of the two components of wind at the 95% confidence level are shown.

each dataset (Fig. 10). The PC1s of the simulations are able to generally capture the temporal evolution of the C-mode index represented by PC2 in the reanalysis. However, the rapid phase switch around late winter in the reanalysis is not reproduced by the models. As the ENSO mode itself is concerned, the PC2s in the models show a shift in the peak time by about three months compared to the reanalysis. The performance of the middle resolution (N216) model is relatively better, of which the PC1 also matches the theoretical C-mode the best (Fig. 3f). This implies that the unrealistic periodic characteristic of the C-mode in the simulation is partly attributable to the distorted ENSO evolution. Therefore, improving the performance of the ENSO signal period in models is crucial to better simulating the C-mode.

Previous studies have pointed out the southward shift of zonal surface wind anomalies is attributable to the meridional seasonal march of western Pacific background warm SSTs and corresponding intensification of the SPCZ due to the seasonal evolution of solar insolation (Harrison and Vecchi, 1999; Spencer, 2004; Lengaigne et al., 2006; McGregor et al., 2012). The reduced climatological wind speed related to the SPCZ intensification leads to anomalous boundary layer Ekman pumping and a reduced surface momentum damping of the combined boundary layer/lower-troposphere surface wind response to El Niño, which allows the associated zonal wind anomalies to shift south of the equator (McGregor et al., 2012). Besides, Ham and Kug (2014) used CMIP3 and CMIP5 archives to reveal that the climatological mean precipitation over the central/eastern Pacific ITCZ plays an important role in ENSO phase transition by affecting the location of the ENSO-related convection and the wind stress. Figure 11 displays the climatological annual evolution of the precipitation over the central Pacific. The models simulate excessive mean precipitation over the ITCZ through late spring to winter. Also, the SPCZ intensification starts in October in the simulation, while in the observation it occurs in

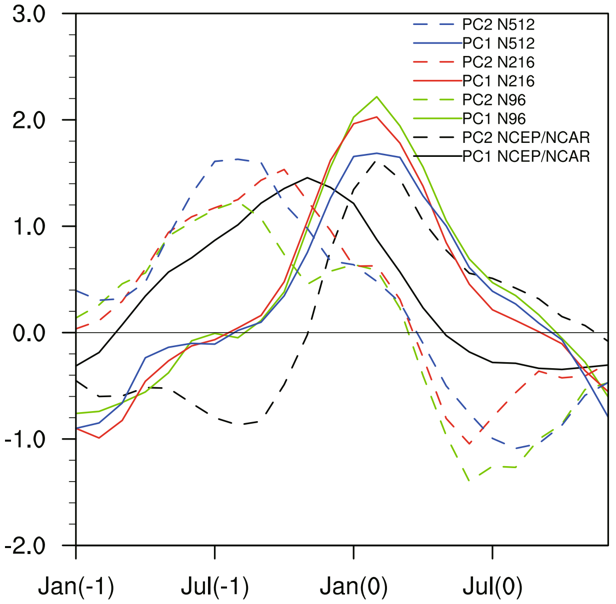

Fig. 10. PC1 (solid) and PC2 (dashed) composites of the El Niño events for the reanalysis and the model results. In the composite, year(0) denotes the developing phase and year(1) the decaying phase.

winter. The unrealistic simulation of the climatological precipitation over the central Pacific could be a factor in the relatively poor representation of the ENSO phase-lock (Fig. 10), and affects the C-mode dynamic process by providing a distorted annual cycle background.

3.3. *Simulated C-mode climate impacts on East Asian rainfall*

Previous studies have indicated the C-mode is essential to the linkage between the East Asian climate and ENSO (Li et al., 2016a; Zhang et al., 2016a, 2016b), especially the Yangtze River summer rainfall (Zhang et al., 2016b). Taking the C-mode signal into consideration could improve the predictability of the summer precipitation in El Niño events. We use the middle resolution (N216) results as an example to check the ability of HadGEM3 to reproduce this connection between the East Asian summer rainfall and ENSO (Fig. 12). Figure 12a demonstrates the average precipitation anomalies in the decaying summer (June–July–August) of the two strongest El Niño events in the N216 simulation, with increased rainfall over the Yangtze River Valley and decreased rainfall over the southeast of China. Using the Niño3.4 index alone can only reconstruct a small fraction of the precipitation anomaly (Fig. 12b). Including the Niño-A index can significantly improve the rainfall reconstruction, especially over the Yangtze River Valley. Therefore, this linkage is reproducible in HadGEM3, which gives us a suggested method to improve the prediction of East Asian summer precipitation associated with ENSO when applying the model outputs.

4. Summary and discussion

In this study, we compare the performance of the UK Met Office Hadley Center's HadGEM3 in representing the ENSO-annual cycle C-mode and the asymmetric SST response with three different resolutions: N96, N216 and N512, respec-

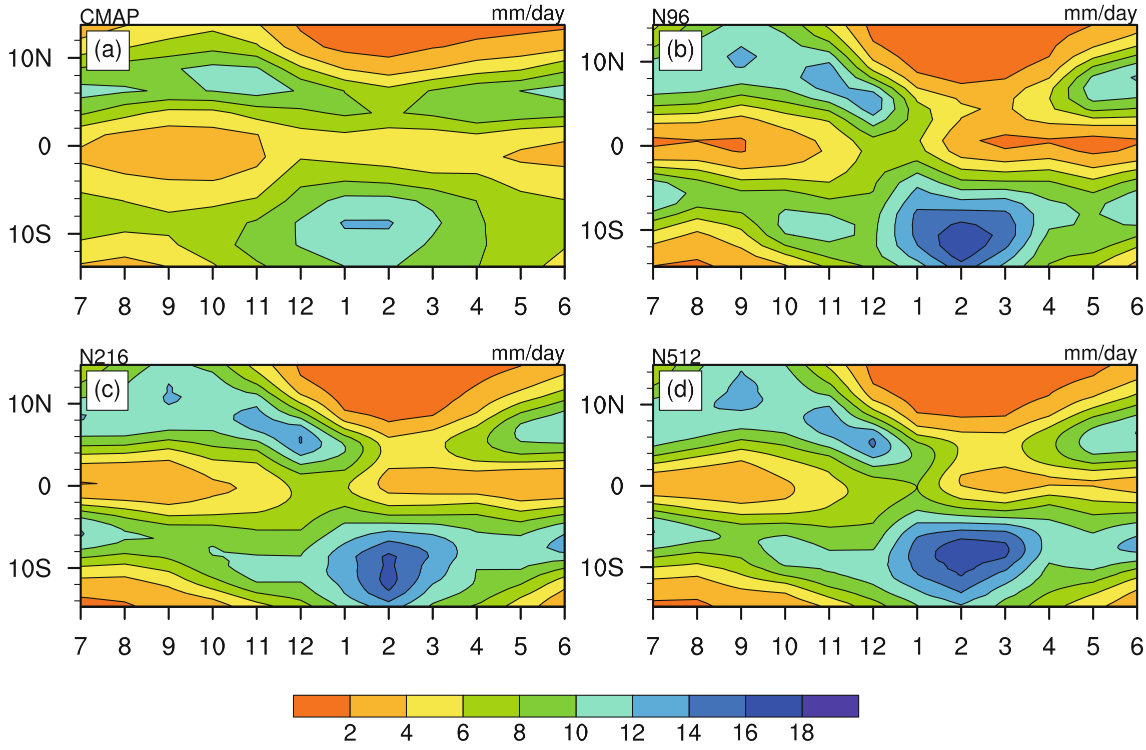

Fig. 11. Climatological annual evolution of the zonal mean (between 160°E and 160°W) precipitation (units: mm d^{-1}) from the CMAP dataset and the model simulation.

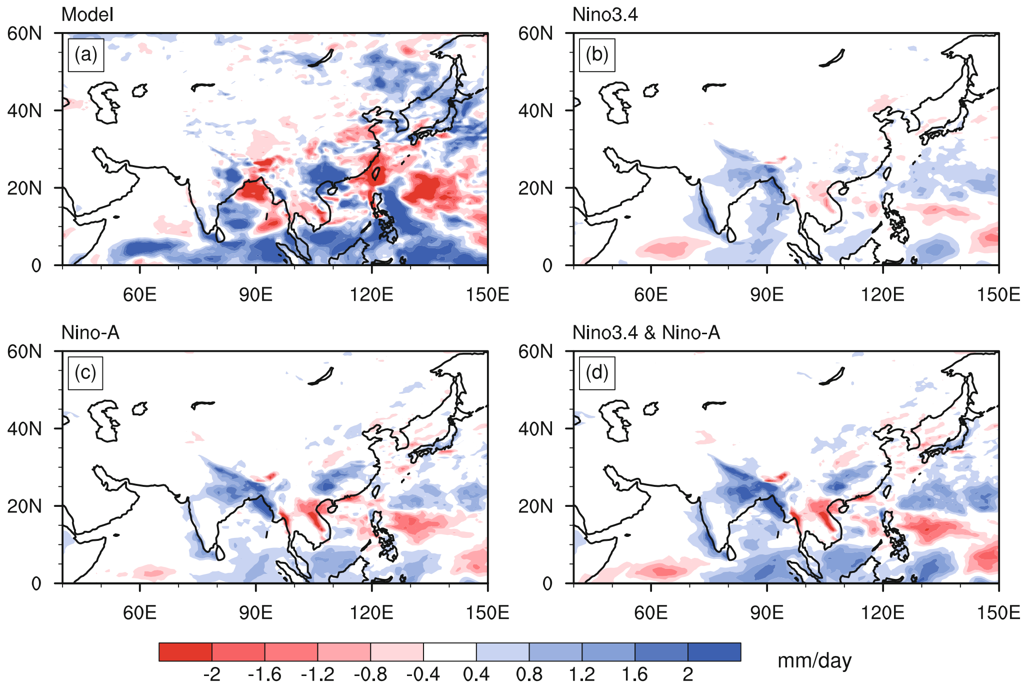

Fig. 12. (a) Precipitation anomalies during the decaying summer of the two strongest El Niño events in the N216 simulation. Reconstruction of precipitation anomalies using linear regression with (b) Niño3.4 index, (c) Niño-A index, and (d) both Niño3.4 and Niño-A indices. Units: mm d^{-1}.

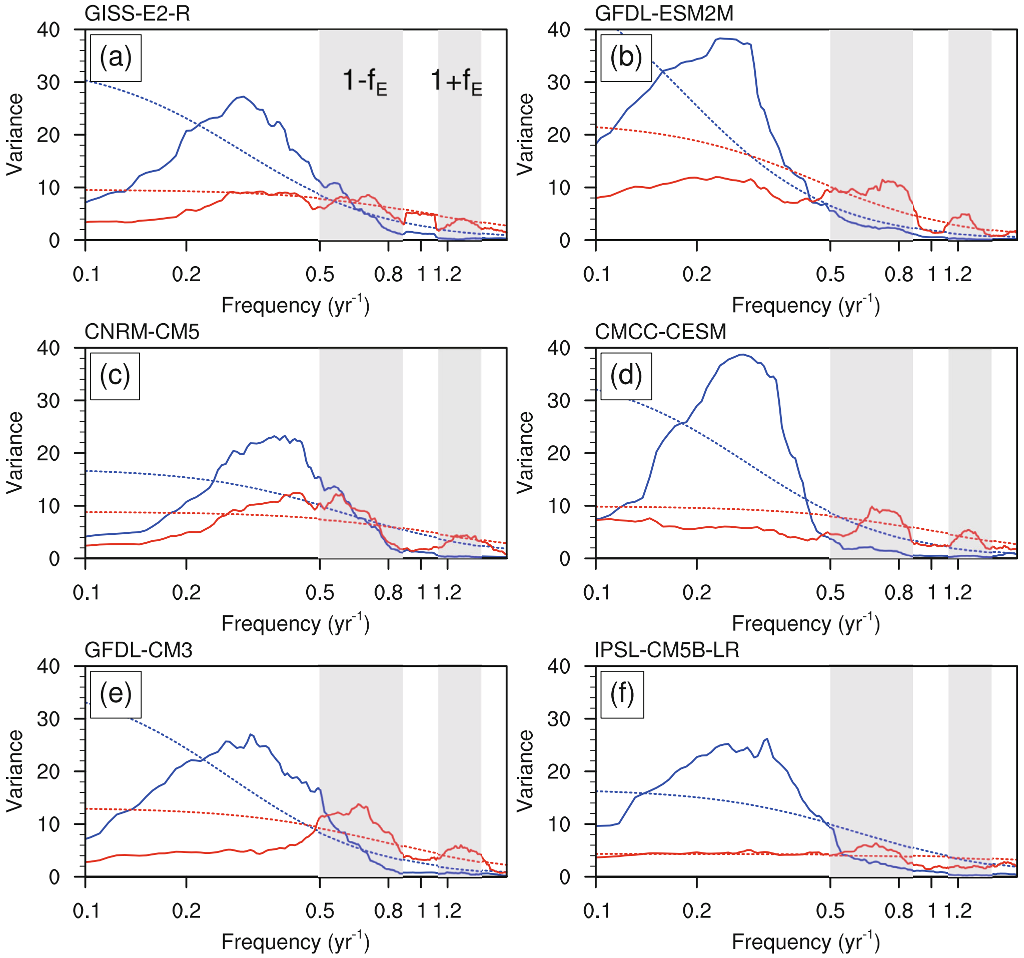

Fig. 13. Spectra curves of PC1 (blue) and PC2 (red) for six models from CMIP5. Dashed lines indicate statistical significance at the 95% confidence level.

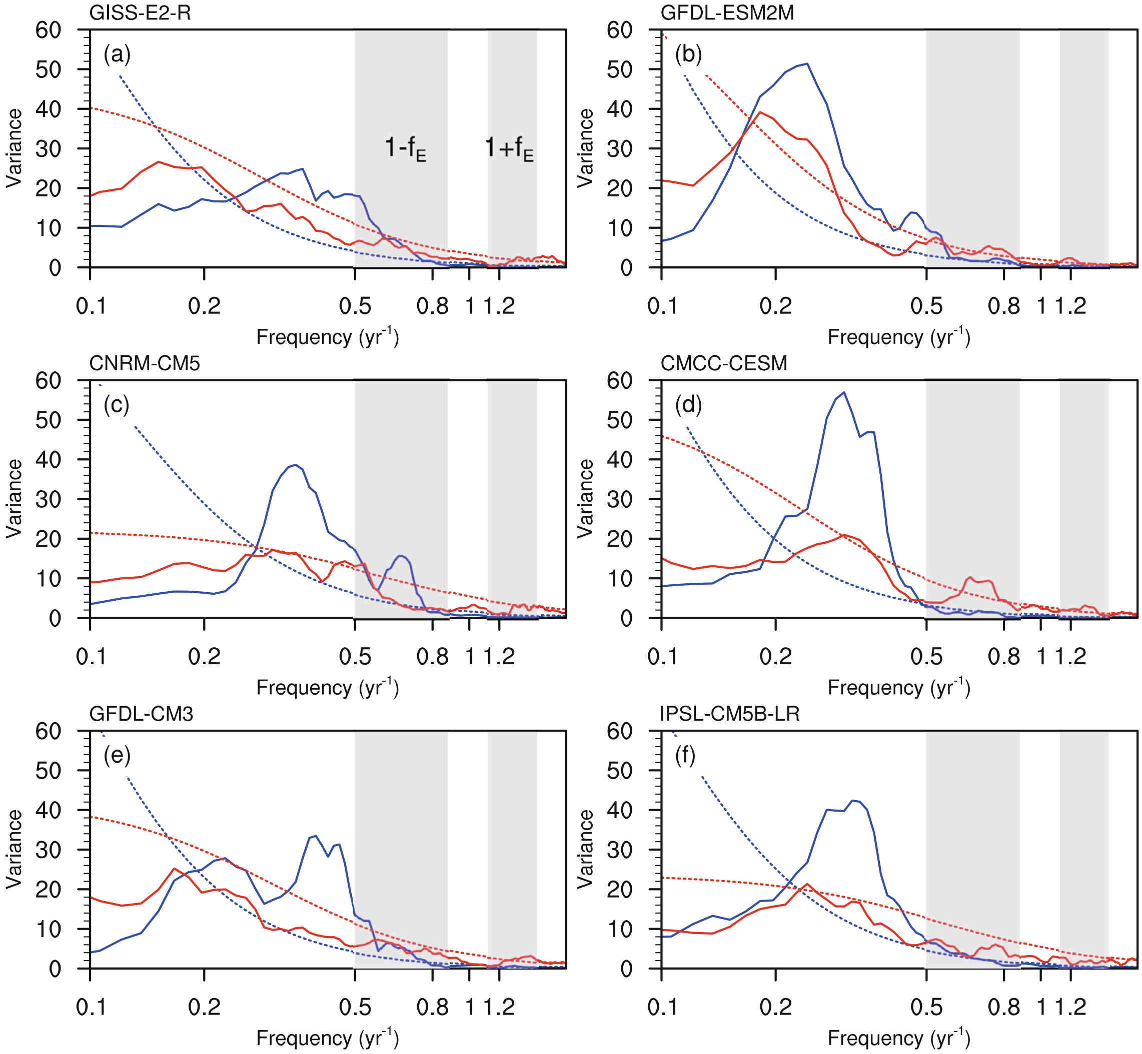

Fig. 14. Spectra curves of standardized Niño3.4 (blue) and Niño-A(red) for six models from CMIP5. Dashed lines indicate statistical significance at the 95% confidence level.

tively. The results indicate that HadGEM3 can capture the spatial characteristics of ENSO and the ENSO-annual cycle C-mode, but it overestimates the C-mode accounted variance such that the C-mode turns into the dominant pattern in the surface wind fields. Meanwhile, the model can reproduce the spectral peaks of the C-mode at periods of about 10 and 15 months, which are the ENSO-annual cycle combined frequency. However, its behavior is not ideal on longer time scales, perhaps due to the relatively unrealistic simulation of the basic ENSO mode with a shorter period and shifted seasonal evolution peak during the El Niño event, which affects the nonlinear coupled process. Also, the model cannot simulate well the rapid PC2 phase transition near late winter. The simulated basic ENSO signal also exhibits a strong signal near the combination frequency both in SST and surface wind variability, implying the model cannot unambiguously tell the difference between the ENSO signal and the C-mode signal.

Ren et al. (2016) compared the atmospheric features of the C-mode simulated by 27 CGCMs from CMIP5, demonstrating that most of them are able to reproduce the spatial pattern of the C-mode well with the correct order of the first two EOFs. Figure 13 illustrates the PC1 and PC2 spectra of the six best performing models in CMIP5, selected according to the correlation coefficients between the observed EOF2 and the simulated EOF2 of the surface wind (Ren et al., 2016). All PC2s show two distinctive combination frequencies without an unrealistic low-frequency peak. The ENSO mode and the C-mode can be distinguished from each other clearly. The circumstances are generaly similar in the oceanic characteristics (Fig. 14), but with relatively weak combination frequency peaks of the Niño-A indices than the PC2s, which is also the case for the observation. These models capture the C-mode better than HadGEM3, possibly because of the more realistic simulation of the ENSO mode.

The C-mode not only plays an important role in the intrinsic dynamical mechanism of ENSO evolution, but also in the process of ENSO affecting climate globally, especially the East Asian summer climate. It is valuable to keep bettering the ability of models in reproducing the C-mode variability, as well as its influences on global climate. To achieve such progress, it is helpful to improve the simulation of the precipitation climatology as well as the basic ENSO variability, including the spatial pattern, the frequency, the temporal evolution, and other properties.

Acknowledgements. This work and its contributors were jointly supported by the China Meteorological Administration Special Public Welfare Research Fund (Grant No. GYHY201506013), the China National Science Foundation (Grant No. 41606019), and the UK–China Research & Innovation Partnership Fund through the Met Office Climate Science for Service Partnership (CSSP) China as part of the Newton Fund.

REFERENCES

Ham, Y. G., and J. S. Kug, 2014: Effects of Pacific Intertropical Convergence Zone precipitation bias on ENSO phase transition. *Environmental Research Letters*, **9**(6), 064008, https://doi.org/10.1088/1748-9326/9/6/064008.

Harrison, D. E., and G. A. Vecchi, 1999: On the termination of El Niño. *Geophys. Res. Lett.*, **26**(11), 1593–1596, https://doi.org/10.1029/1999GL900316.

Hewitt, H. T., D. Copsey, I. D. Culverwell, C. M. Harris, R. S. R. Hill, A. B. Keen, A. J. McLaren, and E. C. Hunke, 2011: Design and implementation of the infrastructure of HadGEM3: The next-generation Met Office climate modelling system. *Geoscientific Model Development*, **4**(2), 223–253, https://doi.org/10.5194/gmd-4-223-2011.

Jin, F.-F., J. D. Neelin, and M. Ghil, 1994: El Niño on the devil's staircase: Annual subharmonic steps to chaos. *Science*, **264**(5155), 70–72, https://doi.org/10.1126/science.264.5155.70.

Kalnay, E., and Coauthors, 1996: The NCEP/NCAR 40-Year reanalysis project. *Bull. Amer. Meteor. Soc.*, **77**(3), 437–472, https://doi.org/10.1175/1520-0477(1996)077<0437:TNYRP>2.0.CO;2.

Lengaigne, M., J.-P. Boulanger, C. Menkes, and H. Spencer, 2006: Influence of the seasonal cycle on the termination of El Niño Events in a coupled general circulation model. *J. Climate*, **19**(9), 1850–1868, https://doi.org/10.1175/JCLI3706.1.

Li, H., W. J. Zhang, and J. H. He, 2016a: Influences of ENSO and its combination mode on seasonal precipitation over eastern China. *Acta Meteorologica Sinica*, **74**(3), 322–334, https://doi.org/10.11676/qxxb2016.025. (in Chinese with English abstract)

Li, H. Y., W. J. Zhang, J. H. He, and Y. L. Wang, 2016b: Influence of SST annual cycle on local air-sea processes during El Niño events. *Haiyang Xuebao*, **38**(1), 56–58, https://doi.org/10.3969/j.issn.0253-4193.2016.01.006. (in Chinese with English abstract)

McGregor, S., A. Timmermann, N. Schneider, M. F. Stuecker, and M. H. England, 2012: The effect of the South Pacific convergence zone on the termination of El Niño events and the meridional asymmetry of ENSO. *J. Climate*, **25**(16), 5566–5586, https://doi.org/10.1175/JCLI-D-11-00332.1.

Rayner, N. A., D. E. Parker, E. B. Horton, C. K. Folland, L. V. Alexander, D. P. Rowell, E. C. Kent, and A. Kaplan, 2003: Global analyses of sea surface temperature, sea ice, and night marine air temperature since the late nineteenth century. *J. Geophys. Res.*, **108**(D14), 4407, https://doi.org/10.1029/2002JD002670.

Ren, H. L., J. Q. Zuo, F. F. Jin, and M. F. Stuecker, 2016: ENSO and annual cycle interaction: the combination mode representation in CMIP5 models. *Climate Dyn.*, **46**, 3753–3765, https://doi.org/10.1007/s00382-015-2802-z.

Ropelewski, C. F., and M. S. Halpert, 1987: Global and regional scale precipitation patterns associated with the El Niño/Southern oscillation. *Mon. Wea. Rev.*, **115**(8), 1606–1626, https://doi.org/10.1175/1520-0493(1987)115<1606:GARSPP>2.0.CO;2.

Senior, C. A., and Coauthors, 2016: Idealized climate change simulations with a high-resolution physical model: HadGEM3-GC2. *Journal of Advances in Modeling Earth Systems*, **8**, 813–830, https://doi.org/10.1002/2015MS000614.

Spencer, H., 2004: Role of the atmosphere in seasonal phase locking of El Niño. *Geophys. Res. Lett.*, **31**, L24104, https://doi.org/10.1029/2004GL021619.

Stein, K., A. Timmermann, N. Schneider, F. F. Jin, and M. F. Stuecker, 2014: ENSO seasonal synchronization theory. *J. Climate*, **27**(14), 5285–5310, https://doi.org/10.1175/JCLI-D-13-00525.1.

Stuecker, M. F., F. F. Jin, and A. Timmermann, 2015a: El Niño-Southern Oscillation frequency cascade. *Proceedings of the National Academy of Sciences of the United States of America*, **112**(44), 13 490–13 495, https://doi.org/10.1073/pnas.1508622112.

Stuecker, M. F., F. F. Jin, A. Timmermann, and S. McGregor, 2015b: Combination mode dynamics of the anomalous Northwest Pacific anticyclone. *J. Climate*, **28**(3), 1093–1111, https://doi.org/10.1175/JCLI-D-14-00225.1.

Stuecker, M. F., A. Timmermann, F. F. Jin, S. McGregor, and H. L. Ren, 2013: A combination mode of the annual cycle and the El Niño/Southern Oscillation. *Nature Geoscience*, **6**(7), 540–544, https://doi.org/10.1038/ngeo1826.

Trenberth, K. E., and J. M. Caron, 2000: The Southern Oscillation revisited: Sea level pressures, surface temperatures, and precipitation. *J. Climate*, **13**(24), 4358–4365, https://doi.org/10.1175/1520-0442(2000)013<4358:TSORSL>2.0.CO;2.

Trenberth, K. E., G. W. Branstator, D. Karoly, A. Kumar, N. C. Lau, and C. Ropelewski, 1998: Progress during TOGA in understanding and modeling global teleconnections associated with tropical sea surface temperatures. *J. Geophys. Res.*, **103**(C7), 14 291–14 324, https://doi.org/10.1029/97JC01444.

Vecchi, G. A., 2006: The Termination of the 1997–98 El Niño. Part II: Mechanisms of atmospheric change. *J. Climate*, **19**(12), 2647–2664, https://doi.org/10.1175/JCLI3780.1.

Wallace, J. M., E. M. Rasmusson, T. P. Mitchell, V. E. Kousky, E. S. Sarachik, and H. von Storch, 1998: On the structure and evolution of ENSO-related climate variability in the tropical Pacific: Lessons from TOGA. *J. Geophys. Res.*, **103**(C7), 14 241–14 259, https://doi.org/10.1029/97JC02905.

Weisheimer, A., and Coauthors, 2009: ENSEMBLES: A new multi-model ensemble for seasonal-to-annual predictions—Skill and progress beyond DEMETER in forecasting tropical Pacific SSTs. *Geophys. Res. Lett.*, **36**(21), L21711, https://doi.org/10.1029/2009GL040896.

Williams, K. D., and Coauthors, 2015: The Met Office Global Coupled model 2.0 (GC2) configuration. *Geoscientific Model Development*, **8**, 1509–1524, https://doi.org/10.5194/gmd-8-1509-2015.

Zhang, W. J., H. Y. Li, M. F. Stuecker, F. F. Jin, and A. G.

Turner, 2016a: A new understanding of El Niño's Impact over East Asia: Dominance of the ENSO Combination Mode. *J. Climate*, **29**(12), 4347–4359, https://doi.org/10.1175/JCLI-D-15-0104.1.

Zhang, W. J., H. Y. Li, F. F. Jin, M. F. Stuecker, A. G. Turner, and N. P. Klingaman, 2015: The annual-cycle modulation of meridional asymmetry in ENSO's atmospheric response and its dependence on ENSO Zonal Structure. *J. Climate*, **28**(14), 5795–5812, https://doi.org/10.1175/JCLI-D-14-00724.1.

Zhang, W. J., and Coauthors, 2016b: Unraveling El Niño's impact on the East Asian Monsoon and Yangtze River summer flooding. *Geophys. Res. Lett.*, **43**(21), 11 375–11 382, https://doi.org/10.1002/2016GL071190.